Can grain size sensitive flow lubricate faults during the initial stages of earthquake propagation?

Nicola De Paola[a*], Robert E. Holdsworth[a], Cecilia Viti[b], Cristiano Collettini[c,d], Rachael Bullock[a].

[(a)]Rock Mechanics Laboratory, Earth Sciences Department, Durham University, South Road, Durham, DH1 3LE, UK.

[(b)]Dipartimento di Scienze Fisiche, della Terra e dell'Ambiente, Siena University, Via Laterina 8, 53100 Siena, Italy.

[(c)]Dipartimento di Scienze della Terra, Sapienza Università di Roma, Piazzale Aldo Moro, 5 – 00185 Roma, Italy.

[(d)]Istituto Nazionale di Geofisica e Vulcanologia, Sezione Roma 1, Via Vigna Murata 605, I-00143 Rome, Italy.

*Corresponding Author: Nicola De Paola, Rock Mechanics Laboratory, Earth Sciences Department, Durham University, South Road, Durham, DH1 3LE, UK.

Tel. +44 (0)191 3342333. E-mail: nicola.de-paola@durham.ac.uk.

Abstract

Recent friction experiments carried out under upper crustal P-T conditions have shown that microstructures typical of high temperature creep develop in the slip zone of experimental faults. These mechanisms are more commonly thought to control aseismic viscous flow and shear zone strength in the lower crust/upper mantle. In this study, displacement-controlled experiments have been performed on carbonate gouges at seismic slip rates (1 ms^{-1}), to investigate whether they may also control the frictional strength of seismic faults at the higher strain rates attained in the brittle crust. At relatively low displacements (< 1cm) and temperatures (≤ 100 °C), brittle fracturing and cataclasis produce shear localisation and grain size reduction in a thin slip zone (150 μm). With increasing displacement (up to 15 cm) and

temperatures (T up to 600 °C), due to frictional heating, intracrystalline plasticity mechanisms start to accommodate intragranular strain in the slip zone, and play a key role in producing nanoscale subgrains (≤ 100 nm). With further displacement and temperature rise, the onset of weakening coincides with the formation in the slip zone of equiaxial, nanograin aggregates exhibiting polygonal grain boundaries, no shape or crystal preferred orientation and low dislocation densities, possibly due to high temperature (> 900 °C) grain boundary sliding (GBS) deformation mechanisms. The observed micro-textures are strikingly similar to those predicted by theoretical studies, and those observed during experiments on metals and fine-grained carbonates, where superplastic behaviour has been inferred. To a first approximation, the measured drop in strength is in agreement with our flow stress calculations, suggesting that strain could be accommodated more efficiently by these mechanisms within the weaker bulk slip zone, rather than by frictional sliding along the main slip surfaces in the slip zone. Frictionally induced, grainsize-sensitive GBS deformation mechanisms can thus account for the self-lubrication and dynamic weakening of carbonate faults during earthquake propagation in nature.

Keywords: Earthquake, Grain Boundary Sliding, Superplasticity, Friction, Viscous Flow, Dynamic Weakening.

1. Introduction

Earthquakes are typically hosted in the shallower portion of crustal fault zones (≤ 15 km depth and ambient $T \leq 300$ °C), where fracturing and cataclasis are traditionally thought to be the dominant processes during frictional sliding (Kohlstedt et al., 1995; Scholz, 1998; Sibson, 1977). At greater depths and temperatures, in the lower crust/upper mantle, viscous flow, potentially associated with superplastic behaviour (Ashby and Verrall, 1973; Boullier and Gueguen, 1975; Hiraga et al., 2010; Rutter et al., 1994; Schmid et al., 1977; Walker et al., 1990), is inferred to facilitate aseismic creep along shear zones, based on experimental data

51 and microstructural observations (Ashby, 1977; Kohlstedt et al., 1995; Passchier, 2005;
52 Poirier, 1985; Rutter, 1995, 1999). Grain boundary sliding (GBS) diffusion creep, associated
53 with superplastic behaviour, i.e., the ability of materials to achieve unusually high elongations
54 (> 100%) before failure, has been observed at high strain rates (> 10^2 s^{-1}) for a range of nano-
55 phase alloys (Chandra, 2002) and ceramics (Lankford, 1996). These mechanisms could
56 potentially occur in ultrafine-grained (nano-scale) geological materials deformed at higher
57 strain rates and temperatures appropriate for seismic slip or slow earthquakes (Green et al.,
58 2015; Rutter and Brodie, 1988; Schubnel et al., 2013; Verberne et al., 2014).
59 Recent laboratory experiments, performed using rotary shear apparatuses, show that when
60 sliding at seismic velocities (≥ 0.5 ms^{-1}) the frictional strength of faults, μ, is significantly
61 lower (μ = 0.1-0.3) (Di Toro et al., 2011; Goldsby and Tullis, 2011; Hirose and Shimamoto,
62 2005; Reches and Lockner, 2010) than when sliding at low (< 1 mms^{-1}), sub-seismic speeds
63 (μ = 0.6-0.85) (Byerlee, 1978). Understanding the processes controlling the evolution of fault
64 strength as seismic slip rates are approached is of paramount importance. Strength cannot be
65 measured directly using seismological data, yet it affects the magnitude of the stress drop, the
66 heat flow signature of seismogenic faults, and the relative partitioning of the earthquake
67 energy budget (i.e., the proportion of energy dissipated as seismic waves that can travel to the
68 Earth's surface and cause damaging earthquakes). It has been proposed that slip weakening of
69 experimental and natural seismic faults is caused by thermally-activated processes triggered
70 by localised frictional heating and high temperatures attained in the slip zone (Rice, 2006).
71 Furthermore, recent studies show that cohesive slip zones (SZs), in natural (Siman-Tov et al.,
72 2013) and experimental carbonate seismic faults (De Paola et al., 2011; Fondriest et al., 2013;
73 Green et al., 2015; Ree et al., 2014; Smith et al., 2013; Verberne et al., 2014), are composed
74 of striated and mirrored slip surfaces (SSs). Microstructural analyses show that the SSs and
75 the adjacent SZ material are made of calcite nanograin (D < 1 μm) aggregates with a

76 polygonal texture, a microstructure consistent with deformation by creep deformation
77 mechanisms. The use of mirror SSs and nano-granular SZ textures as indicators of seismic
78 slip on faults in carbonates (e.g. Ree et al., 2014; Smith et al., 2013) has been questioned by
79 Verberne et al. (2013, 2014) who have shown that similar features can develop during low
80 velocity (1 μms^{-1}) friction experiments performed on simulated calcite gouge at upper crustal
81 P-T conditions. However, the grain-scale processes suggested to account for the observed
82 weakening of rocks deformed in the laboratory at seismic velocities are still debated (De
83 Paola et al., 2011; De Paola, 2013; Han et al., 2010; Tisato et al., 2012), as is their occurrence
84 along natural faults during earthquake propagation. Verberne et al. (2014) performed
85 microstructural analyses on experimentally deformed samples at sub-seismic slip rates (1
86 μms^{-1}) and low temperatures (<140 °C). They show that nanofiber formation during
87 nanogranular flow with diffusive mass transfer can promote velocity-weakening behaviour
88 and earthquake nucleation in carbonate rocks. Green et al. (2015) integrated microstructural
89 observations and experimental work to show that mineral phase transformation in carbonate
90 rocks, occurring at the high temperatures produced by frictional heating, can generate
91 nanometric materials which are weak at seismic slip rates ($\approx 1\ ms^{-1}$) and flow by grain-
92 boundary sliding mechanisms.
93 Here we study the evolution of deformation mechanisms, and their control on the frictional
94 strength of slip zones developed in simulated, carbonate gouges during accelerating sliding to
95 seismic slip rates ($v = 1\ ms^{-1}$). To do so we combine results from new laboratory friction
96 experiments with microstructural observations on samples sheared up to the attainment of
97 dynamic weakening, but *prior* to the onset of phase transformation. Flow stress calculations
98 are performed to investigate whether grainsize-sensitive creep deformation mechanisms,
99 potentially associated with superplastic behaviour, can effectively weaken faults and facilitate
100 earthquake propagation in the shallow crust. To illustrate the relevance of our findings to

101 natural faults, we also carried out microstructural observations on the principal slip zone
102 material extracted from natural, seismically active faults in carbonates.

103 **2. Experimental settings**

104 Friction experiments were performed in the Rock Mechanics Laboratory, at Durham
105 University (UK), using a low to high velocity rotary shear apparatus (details in
106 Supplementary Information 1 – Figure SI1) built by the Marui & Co., Ltd Company (Osaka,
107 Japan). We performed a set of eight displacement-controlled experiments at room temperature
108 and humidity conditions on fine-grained ($63 < D < 93$ μm), carbonate gouges at target slip
109 rates $v = 1$ ms^{-1} and normal σ_n = 12-18 MPa (Supplementary Information – Table I). During
110 displacement-controlled experiments, arrested at pre-determined displacements, the electric
111 servomotor of the apparatus was controlled in the digital mode, using a signal generator
112 DF1906 (NF corporation) (Supplementary Information 1).

113 A synthetic fault zone was created by sandwiching 2 g of simulated fault gouge between
114 two stainless steel cylinders (25 mm in diameter), whose ends were machined with radial
115 grooves 500 μm high to grip the sample surface (Supplementary Information 1 – Figure SI2).
116 The experiments were run under drained conditions, and to limit gouge loss during the
117 experiments, the sample assembly was confined using a Teflon ring. Teflon rings were cut
118 and tightened onto the stainless steel cylinder using a hose clamp. The inner edges of the rings
119 were machined to reduce their sharpness, and thus avoid ring damage and sample
120 contamination by Teflon during the insertion of the stainless steel cylinders (Supplementary
121 Information 1 – Figure SI2).

122 Samples were recovered after each experiment to study the slip zone microstructures. Thin
123 sections for optical microscope observations were taken from slices of the slip zone cut at 2/3
124 of the radius, to make observations consistent with calculated values of the velocity, v, and
125 the displacement d (Supplementary Information 2).

3. Mechanical data

To identify the mechanisms controlling the evolution of friction, we performed a set of displacement-controlled experiments, with a target speed v = 1 ms^{-1}, normal stresses σ_n = 12-18 MPa, and arrested at displacements d from 0.007 to 1.46 m (Supplementary Information Table I). Experiments arrested at different displacements show similar acceleration paths (Fig. 1a-b), showing that the conditions during our experiments are reproducible (Fig. 1c-d). It also means that microstructures developed at different stages/displacements can be used to study the evolution of deformation mechanisms in the slip zone, and how these may affect frictional strength evolution.

During experiments run up to 1.44 - 1.46 m total slip, the imposed target speed of 1 ms^{-1} was attained after 0.12 m of slip (Figs. 1a-b). The measured strength consistently showed a four stage evolution (e.g. Exp. Du304-307 in Figs. 1c-d, Supplementary Information Table I): Stage I) attainment of initial friction values, μ_i = 0.67, upon instantaneous acceleration toward target speed; Stage II) increase in friction up to peak values μ_p = 0.80–0.88, attained just before acceleration to target speed was complete; Stage III) sudden decrease in friction to low steady-state values, μ_{ss} = 0.17-0.21, attained during sliding at constant velocity v = 1 ms^{-1}; and Stage IV) sudden increase of friction to μ_f = 0.44 - 0.45, observed upon deceleration of the motor.

The temperature rise produced during the laboratory experiments has been estimated, to a first approximation, using (Rice, 2006)

$$\Delta T = \frac{\mu \sigma_n \sqrt{vd}}{\rho c_p \sqrt{\pi \kappa}} \qquad \text{Eq. 1}$$

where μ represents the friction coefficient, σ_n is the normal stress, d is the displacement, ρ is the rock density, c_p is the specific heat capacity and κ is the thermal diffusivity. Microstructural evidence for slip localisation within slip zones with thickness h < 150 μm satisfies the condition $h \leq 4\sqrt{\kappa d/v}$, which allows to treat the slip zone as a plane of zero

151 thickness and account for heat diffusion using Eq. 1. For experiments in which steady-state
152 conditions were attained (e.g., Du304 and Du307 in Fig. 1c-d), temperatures were calculated
153 up to the displacements, d_{tr}, attained at the end of the steep drop in friction observed during
154 the transient stage of friction evolution to low, steady-state values, e.g., at d_{tr} = 0.23-0.08 m
155 (Table I). The contribution to temperature increase by sliding from peak friction values to
156 those attained at d_{tr} was calculated by using the mean value for μ in Eq. 1. The following
157 physical properties of calcite, the main mineralogical component in the deformed rocks, were
158 used for temperature calculations: ρ = 2700 kg/m^3, $\kappa = 1.48*10^{-6}$ m^{2}s^{-1} and c_p = 700 J kg^{-1} °K^{-1}
159 (Di Toro et al., 2011 and references therein). The mechanical parameters d, μ, σ_n and v used
160 for the temperature calculations are those reported in Supplementary Information Table I, and
161 the temperatures calculated by Eq. 1 are plotted vs. the measured friction coefficients in Fig.
162 2. It is observed that friction values are in accord with the range of values predicted by
163 Byerlee's rule for temperatures ≤ 554 °C (μ_f = 0.68-0.80), but significantly lower (μ_{ss} = 0.17-
164 0.21) when $T \geq$ 979 °C (Fig. 2).

165 **4. Microstructural Observations and Interpretations**

166 **4.1 Experimental faults**

167 Samples deformed during Stage I (d = 0.007-009 m, Fig. 1c-d) show the formation of an
168 irregular slip zone (SZ) and rough slip surface (SS), due to the presence of grooves (up to 25
169 μm wide) and ridges, oriented parallel to the slip direction (Fig. 3a). A sharply defined,
170 irregular slip surface (SS) bounds the upper part of the SZ, showing variable thickness (20-
171 200 μm), whilst the lower bound between the SZ and less deformed material is sharp, but
172 rather irregular and wavy (Fig. 3b). The SS is heterogeneous, displaying smooth compact
173 areas interspersed with more granular porous areas (Fig. 3a). The granular portions of the SS
174 appear to be coarser in grain size ($10 < D < 25$ μm) compared to the smooth regions. The
175 smooth portions of the SS are made of fine-grained clasts ($1 < D < 5$ μm), which are sharply

truncated against the SS (Fig. 3c). The shape of the clasts on the SS and in the SZ below the SS, is typically angular to sub-angular (Fig. 3c). In places, the smaller clasts display a sub-rounded shape. In the smooth and compact patches, the SS and SZ are still porous, but the porosity, like the grain size, seems finer. Overall, the SZ contains coarse- and fine-grained ($1 < D < 5$ μm), angular clasts, likely formed by brittle fracturing and cataclasis during frictional sliding at low temperatures < 100 °C (Fig. 2).

During Stage II, samples show the development of a cohesive SZ, <150 μm thick (Fig. 4a), containing multiple SSs sandwiching thin layers (tl, ≈ 5 μm) of sub-rounded nanograins (Fig. 4b-c). TEM analyses show that tl contain slightly larger clasts of calcite ($D \leq 1$ μm) dispersed within a porous assemblage of calcite nanograins, ≤100 nm in size, with sub-rounded crystal shapes (Fig. 4d). The calcite clasts host dislocations, locally arranged to form dislocation walls separating subgrains ($D \leq 100$ nm) with small angular misorientations; this is typical of low temperature (≤ 600 °C) intragranular dislocation creep deformation (Rutter, 1995) (Fig. 4d). Bright-field TEM images show that, together with dislocation walls and subgrain boundaries, calcite clasts (CC) exhibit "damaged" rims, hosting rounded bubbles and lobate, low-contrast features (Fig. 4e). These nanostructures suggest concomitant decarbonation and amorphization processes, preferentially located within the strained calcite rims and at subgrain boundaries. This is where crystal structure defects are concentrated and where, it is suggested, calcite becomes more reactive. We propose that the occurrence of an amorphous phase along subgrain boundaries will facilitate clast disaggregation and the subsequent formation of nano-sized, calcite grain aggregates (Fig. 4d-e). The d-spacing measurements, obtained from the ring-shaped Selected Area Electron Diffraction (SAED) pattern of ultrafine-grained material, confirm that ultrafine grains are composed of calcite (Fig. 4f). In particular, rings I and II correspond to 3.82 and 3.00 Å spacing (Fig. 4f), in strong agreement with the 3.85 and 3.03 Å of reference calcite (012 and 104 reflections, respectively).

When deforming through Stage III, up to d = 1.44-1.46 m (Fig. 1c-d), samples show the localisation of slip in a cohesive SZ, < 150 mm thick, and the formation of shiny, mirror-like SS's (Fig. 5a). The bulk slip zone configuration is similar to those seen during Stage II (Fig. 4a-b), but the grain scale textures are very different. Low porosity SS's ($D \approx$ 600-700 nm) separate thin layers of nanograin ($D \approx$ 100-600 nm) aggregates with markedly polygonal textures and straight grain boundaries (Fig. 5b-c). SEM images show that the SS's and the thin layers (tl) are composed of relatively compact, polygonal nanostructures of calcite grains, with 120° triple junction contacts between equiaxial grains (Fig. 5b-c). Patches of polygonal nanograins with coarser (600-700 nm, Fig. 5b) and finer (≤ 100 nm, Fig. 5c) grainsize are observed in the tl, in contrast to the polygonal nanograins on the SS which display a more uniform, but larger grainsize distribution (600-700 nm) (Fig. 5b-c). TEM analyses show that the finer and coarser calcite grains in the tl have low dislocation densities, as shown by their homogeneous TEM contrast, regardless of their crystal orientation (Fig. 5d). Relatively large cavities (e.g., C in Fig. 5e) occur along grain boundaries or at triple junctions, whereas smaller rounded bubbles are trapped within calcite grains (Fig. 5e). Calcite clasts from the tl in the SZ exhibit irregular, lobate crystal boundaries, surrounded by thin (<10 nm) rims of amorphous material of limited extent (Fig. 5f). Calcite grains do not show crystal preferred orientation, as they are characterized by ring-shaped SAED patterns (Fig. 5g). Measured d-spacing confirms that the polygonal grains are calcite (Fig. 5g).

4.2 Phase transformation and annealing processes

We found little evidence for phase transformations that might cause weakening in our experiments. Microstructural and mineralogical observations show that the development of degassing bubbles (Figs. 4e, 5e) and amorphization rims (Figs. 4e, 5f), indicative of decarbonation reactions, are limited to the boundaries of calcite grains in the SZ of samples deformed through Stage II and Stage III. In both cases, SAED pattern analyses revealed that

the clasts in the SZ are composed of calcite (Figs. 4f, 5g), confirming that decarbonation reactions in the SZ of samples deformed up to Stage III were not quantitatively significant. We interpret this as being due to the kinetics of the decarbonation reaction requiring exposure to decomposition temperatures for periods much longer than the few fractions of a second that occurred during our experiments (De Paola et al., 2011a). This interpretation is supported by further microstructural evidence showing that widespread and pervasive, intragranular thermal decomposition processes do affect polygonal calcite grains, when high temperatures are maintained for longer time periods (> 2 s) during high displacement experiments (d > 5m) (Supplementary Information 2). Thus we propose that the observed weakening is not caused by thermally activated phase transitions when fault displacements are < 1.5 m.

Microstructural observations on samples deformed up to Stage III show the presence of localised patches of small (≤ 100 nm) polygonal nanograins in the tl of the SZ. The grainsizes are similar to those observed in the tl of samples deformed up to Stage II (Figs. 4b-d, 5b-c). However, slightly larger polygonal nanograins (600-700 nm) have also been observed on both the SS and in the tl of samples deformed up to Stage III (Fig. 5b-c), suggesting that grain growth processes occurred in the nanograins of the experimental SZ. Grain growth kinetics and the grainsize that can be attained by normal grain growth are described by the well know equation (e.g., Covey-Crump, 1997)

$$d^{\frac{1}{n}} - d_0^{\frac{1}{n}} = k_0\, t e^{-\frac{H}{RT}} \qquad \text{Eq. 2}$$

where d is the grainsize, d_0 is the initial grainsize, t is the duration of the growth period, n is a dimensionless constant which depends on the process controlling the growth rate, k_0 is the pre-exponential factor, H is the apparent activation enthalpy of the process controlling the grain growth, R is the gas constant and T is the temperature. During sample deformation up to Stage II (T = 500 °C) and Stage III (T = 800-1000 °C) (Supplementary Information Table 1), the maximum temperatures inferred in the slip zone are only attained for a fraction of a

second, and it takes < 10 s for our sample to cool down to $T < 100$ °C. Hence, we assume that $t = 1$ s is a conservative estimation of the time-scale upon which grain growth, due to static recrystallization, may occur in the slip zone. The parameters $n = 0.5$, $k_0 = 3.5502 * 10^{-10}$ $\mu m^{1/n}$ s^{-1} (obtained from $k_{979\,°K} = 5.5626 * 10^{-3}$ $\mu m^{1/n}$ s^{-1}), $H = 240 * 10^3$ J mol^{-1}, $R = 8.3145$ J $°K^{-1}$ mol^{-1}, obtained by Covey-Crump (1997) for the pore-fluid absent conditions, were used to solve Eq. 2, and to calculate the maximum theoretical increase in grain size, d, from an initial grain size $d_0 = 0.1$ μm, when growth time $t = 0.1$, 1, 10 s and temperature $T =$ 500, 800, 900, 1000 °C (Fig. 6). The results show that, for conditions similar to those attained in samples deformed up to Stage II (e.g. $T = 500$ °C and initial grain size $d_0 = 0.1$ μm), no grain growth should occur in our samples (Fig. 6). Under these conditions, the activation of grain boundary migration processes requires timescales significantly longer than the overall duration and quenching phase of our experiments (Fig. 6). These results agree well with our microstructural observations on SS and tl nanograin aggregates showing $D \leq 100$ nm and a lack of diagnostic large and dislocation-free grains that would be expected to form during annealing.

For conditions similar to those attained in samples deformed up to Stage III (e.g. $T =$ 800-1000 °C and initial grain size $d_0 = 0.1$ μm), grain growth is predicted to occur for the range of time 0.1 s $\leq t \leq$ 10 s considered (Fig. 6). At these conditions, grain boundary migration processes could be activated within 0.1 s from the attainment of the high temperatures reached in our experiments when deformed up to Stage III (Fig. 6). Our microstructural observations of polygonal, nanograin aggregates on the SS and in the tl show grain growth from initial values of $d_0 \leq 100$ nm up to $D =$ 600–700 nm, which is lower than the maximum grainsize $d = 2.25$ μm predicted by grain growth calculations at $T = 1000$ °C and $t =$ 1s (Fig. 6). TEM analyses show that the polygonal calcite grains do have low dislocation density, but there is still a lack of diagnostic large and dislocation-free grains, which would be expected to

form during complete annealing. We conclude that static recrystallization and growth of the nanograin aggregates on the SS and within localised patches in the tl may have occurred after the experiments, during the cooling stage of samples deformed up to Stage III, although the integration of microstructural and theoretical data show that grain growth may only have caused a partial annealing of the original fabric. Elements of this fabric may still be preserved in the tl as patches of fine grainsize polygonal nanograins (see Fig. 5c). The attainment of high T for short durations ($t \leq 1$ s) and the presence of second-phase materials (e.g., amorphous decomposed material, Fig. 5f) and pores (e.g., degassing bubbles, Fig. 5e) pinning the grain boundaries (Olgarard and Evans, 1986), may have limited grain growth during our experiments. This plausibly explains the local preservation of patches of finer polygonal nanograins and the lower grainsizes observed than those theoretically predicted (Fig. 6).

5. Natural faults

In the last decade a series of studies have documented the nucleation and/or propagation of significant earthquakes through thick sequences of carbonates (e.g. Miller et al., 2004; Valoroso et al., 2014). Motivated by these observations, several workers have focussed on the study of carbonate-bearing faults exhumed from the seismogenic crust in order to improve the characterization of fault zone structure and deformation processes (e.g. De Paola et al., 2008; Smith et al., 2011; Rowe et al., 2012; Collettini et al., 2013; Siman-Tov et al., 2013; Bullock et al., 2014). Here as a natural example, we use a large-offset (≈ 600 m) fault exposed in the seismic belt of the Apennines, Italy. The fault is 10 km long with a maximum width of about 1.5 km and consists of 5 sub-parallel segments (Collettini et al., 2014). At the outcrop scale the fault structure is characterized by striated and mirrored SS's (Fig. 7a), similar to those observed in other carbonate-hosted, seismically active faults (Smith et al., 2013, Siman-Tov et al., 2013). Sampling and microstructural studies across the SS reveal a natural cohesive SZ (<150 μm thick) characterized by parallel SS's (Fig. 7b, c).

SEM investigations of the SZ show calcite grains with lobate and faint grain boundaries. Grain boundaries are characterized by the concentration of voids and/or vesicles, indicating limited thermal decomposition of calcite (Fig. 7b and Collettini et al., 2014). TEM analyses show that some portions of the SS's and the SZ material are made of micrometer-sized calcite crystals, which commonly show nanoscale polysynthetic twinning. High dislocation densities and subgrain boundary formation indicate that twin lamellae have experienced intense strain. The pervasive occurrence of subgrain boundaries along twinning planes suggests that twinning predates the development of dislocations, dislocation walls and calcite nanograins (D = 200-300 nm). Other portions of the SS's and SZ material show calcite nanograin ($D \leq$ 100 nm) aggregates with a polygonal texture; the nanograins have straight grain boundaries with 120° triple junction contacts between equiaxial grains, and display no preferred elongation (Fig. 7d). These natural microstructures are strikingly similar to those observed in the experimentally deformed samples during Stage III (Fig. 5c).

6. Discussion

6.1 Micro-scale deformation mechanisms during earthquake propagation

In the experimental samples, a localised slip zone, up to 150 μm thick, develops in the early stages of deformation (Stage I) when the SZ material is poorly consolidated, bounded by slip surfaces, and made of fine-grained, angular clasts ($1 \leq D \leq 5$ μm). Brittle fracturing and cataclasis are the dominant deformation mechanisms observed in samples deformed up to Stage I, at relatively low temperatures (≤ 100 °C), and it is these mechanisms that likely control shear localisation and grain size reduction in the slip zone (Fig. 3) (Bullock et al., 2015; Smith et al., 2015). In our experiments — unlike those of Verberne et al. (2014) — we do not observe the development of shiny, mirror-like slip surfaces and of nanoscale materials in the SZ of samples deformed up to Stage I (up to 7 mm slip). Sliding friction values

predicted by Byerlee's rule (Byerlee, 1978) match those measured during experiments arrested in Stage I (Fig. 1).

SEM analyses of samples deformed up to Stage II show that the SZ material becomes cohesive and contains multiple SS's, which sandwich thin (≈ 5 μm) porous layers of sub-rounded nanograins (Fig. 4). TEM analyses show larger clasts of calcite ($D \approx 1$ μm) dispersed within a porous assemblage of calcite nanograins, ≤ 100 nm in size. These larger calcite clasts exhibit a high density of free dislocations and host subgrains ($D \leq 100$ nm) (Fig. 4d-e). As temperatures rise during Stage II, due to frictional heating (T ≈ 550 °C), intracrystalline plasticity mechanisms, active at T ≤ 600 °C, start to accommodate intragranular strain and the development of nanoscale subgrains ($D \leq 100$ nm) in the thin layers of the slip zone (Fig. 4d-e).

When deformation progresses through Stage III, samples show a bulk slip-zone configuration similar to Stage II, but the grain-scale microstructures are very different. SEM and TEM analyses of thin layers of nanograin (D ≈ 100-600 nm) aggregates between the SS's exhibit polygonal grain boundaries, showing 120° triple junctions between equiaxial grains (Fig. 5b-e). The grains display no preferred elongation, no crystal preferred orientation (based on SAED measurements) and low dislocation densities (Fig. 5d-g), possibly due to high temperature (≥ 900 °C) GBS deformation mechanisms. The observed micro-textures in experimental (Fig. 8a) and natural slip zones (Fig. 8b) are strikingly similar to those predicted by theoretical studies (Fig. 8c, Ashby and Verrall, 1973), and those observed during experiments on metals (Chandra, 2002) and fine-grained carbonates (Walker et al., 1990, Schmid et al., 1977), at temperatures ≤ 1000 °C, where superplastic behaviour due to grainsize-sensitive GBS has been inferred. Hence, we propose that the preservation of equiaxial polygonal nano-grains (D ≤ 100 nm), with low dislocation densities, is diagnostic of GBS mechanisms associated with superplastic behaviour (Verberne et al., 2013, 2014).

Our SEM and TEM observations show that the synthetic carbonate gouges deformed up to Stage III in our experiments preserve microstructural evidence for the operation of GBS accommodated by *both* diffusion and dislocation creep (Fig. 5c-e). The polygonal nanograins developed during Stage III are characterized by a much lower dislocation density compared to those observed during Stage II. This may be due to the establishment of less favourable conditions for the operation of dislocation creep (i.e., high T, small grain size) attained at the transition from Stage II to Stage III in our experiments. Despite microstructural evidence for the simultaneous occurrence and operation of both diffusion- and dislocation-dominated GBS, more microstructural work is needed to quantify their relative contribution to the deformation of nanoscale materials at high strain rates and temperatures. Overall, the distinctive textures observed indicate a switch from low-temperature plasticity and cataclasis (Stages I, II) to GBS mechanisms (Stage III).

Finally, we suggest that the re-strengthening observed during deceleration at the end of the friction experiments (Stage IV, Fig. 1c-d) results from a decrease in the activity of slip zone-localised GBS associated with decreasing temperatures.

6.2 Slip zone strength: can grain size sensitive creep control fault strength during earthquake propagation?

Our experimental results and microstructural observations reveal evidence for the operation of both intracrystalline plasticity and GBS-accommodated flow processes in slip zones deformed at earthquake velocities. The evolution of distinctive micro-textures observed in the slip zone suggests that the transition from low-temperature plasticity and cataclasis ($T \leq$ 500 °C during Stages I and II, Figs. 2-4) to GBS-accommodated flow ($T \geq$ 800 °C during Stage III, Figs. 2,5,8) coincides with the onset of the weakening measured in the tested materials at seismic conditions (Figs. 1-2). Verberne et al. (2014) were the first to speculate that GBS-accommodated flow could occur at high strain rates and temperatures during

375 rupture propagation in carbonate rocks. Green et al. (2015) produced further experimental
376 evidence for the occurrence of phase transformation and GBS-accommodated flow in
377 carbonate rocks shearing at seismic slip rates and temperatures, and proposed that these
378 mechanisms could be associated with the onset of dynamic weakening in carbonate rocks. In
379 our experiments, phase transformations, such as decarbonation of calcite, that might lead to
380 weakening are of limited extent. Hence, whilst we agree with the previous hypotheses that
381 GBS-accommodated flow can weaken faults at seismic slip rates (Green et al., 2015;
382 Verberne et al., 2014), we suggest that the onset of the observed weakening does not require
383 thermally-activated phase transitions to occur in carbonate rocks.
384 We now calculate flow stresses to add new evidence to the hypothesis that GBS-
385 accommodated flow can weaken faults at high strain rates and temperatures, prior to the onset
386 of phase transformations, and thus control earthquake propagation in the shallow crust. We
387 use published constitutive flow laws for both dislocation creep and diffusion-dominated GBS
388 in carbonates at temperatures ≥ 500 °C (Ashby and Verral, 1973; Schmid et al., 1977; Walker
389 et al. 1990), applying a range of strain rates and grain sizes representative of our experimental
390 conditions (Supplementary Information Table I).
391 **6.2.1 Flow laws and state variables**
392 The predicted flow stress for end-member type deformation mechanisms, dislocation creep
393 and diffusion creep, can be modelled by the constitutive flow law
394 $$\dot{\gamma} = A^* D^{-b} e^{-\frac{H}{RT}} \tau^n \qquad \text{Eq. 3}$$
395 where $\dot{\gamma}$ is the shear strain rate, A^* is a pre-exponential factor, H is the apparent activation
396 energy for creep, R is the gas constant, T is the absolute temperature, τ is the shear stress, n
397 the stress exponent, D is the grain size and b is the grain size exponent. For dislocation creep,
398 b is 0 and $3 < n < 7$, whereas for diffusion creep (which must include GBS) $2 < b < 3$ and $n =$
399 1. For dislocation-accommodated GBS, b and n lie somewhere between these two end

members, so that $1 < n < 3$ values are predicted for grainsize-sensitive creep regimes (Ashby and Verral, 1973), when the superposition of the two end-member mechanisms accommodates viscous flow (Ashby and Verral, 1973; Schmidt et al., 1977). In the latter case ($1 < n < 3$), the overall creep rate should be given, to a sufficient approximation, by their relative contribution (Ashby and Verral, 1973).

The parameters $b = 0$, $n = 4.70$, $A = 0.046$ (s^{-1} bar^{-n}), $H = 71$ (kcal $mole^{-1}$), $R = 1.987*10^{-3}$ (kcal °K $mole^{-1}$), and $b = 3$, $n = 1.7$, $A^* = 9.55*10^4$ ($s^{-1}bar^{-n}$), $H = 51$ (kcal $mole^{-1}$), $R = 1.987*10^{-3}$ (kcal °K $mole^{-1}$), obtained for deformed calcite aggregates from Schmid et al. (1977), were used to solve Eq. 3 and to calculate the flow stress t predicted for dislocation creep and grainsize-sensitive GBS-accommodated flow, respectively, when $T = 600$, 1000 °C and $\dot{\gamma} = 1 - 3*10^3$ s^{-1} (Fig. 9).

The average shear strain, γ, values have been calculated by $\gamma = \tan \phi = r\theta/2h$, where ϕ is the angular shear, r is the outer diameter of the sample, θ is the angular displacement in radians and h is the average slip zone thickness. Shear strain rate, $\dot{\gamma}$, can then be calculated as the ratio $\dot{\gamma} = \Delta\gamma/\Delta t$, where Δt is the duration of each experiment from the onset of a specific deformation mechanism. An average value, $h = 150$ μm, has been assumed during shear strain calculations, based on optical and scanning electron microscope images, which show the development of a slip zone, due to shear localisation, from the very early stages of deformation when d is only a few mm (Fig. 3a). Strain rate values calculated for each deformation mechanism observed during the different stages of the experiments have been used as reference values during the flow stress calculations (Fig. 9, Table I). The grain size range $D = 10$-600 nm was used during flow stress calculation of grainsize-sensitive GBS-accommodated flow, based on microstructural observations of the slip zone material produced during Stage II and Stage III deformation (Figs. 4-5).

6.2.2 Flow stress values and interpretation of results

425 Flow stress calculations, performed using Eq. 3, show that dislocation creep mechanisms
426 operate at higher flow stress values (τ > 100 MPa) than grainsize-sensitive GBS in the range
427 of temperatures (T = 600-1000 °C) and strain rates ($\dot{\gamma}$ = 1-3*10^3 s^{-1}) considered, when grain
428 size D < 600 nm (Fig. 9). For a given temperature, the flow stress increases with strain rate at
429 a steeper gradient during GBS than during dislocation creep (Fig. 9). For a given temperature
430 and a fixed strain rate, the flow stress due to GBS decreases with grain size (Fig. 9). At T =
431 600 °C and high strain rates ($\dot{\gamma} \geq 1000$ s^{-1}), the two mechanisms would operate at similar, very
432 high flow stress values ($\tau \approx 3000$ MPa) for a grain size of about 100 nm (Fig. 9a). Under these
433 conditions, the calculated flow stress values are always significantly higher than the values
434 measured during our laboratory experiments (Fig. 9a). At T = 1000 °C and high strain rates ($\dot{\gamma}$
435 ≥ 1000 s^{-1}), grainsize-sensitive GBS flow would operate at much lower flow stress values ($\tau \leq$
436 12 MPa) than dislocation creep ($\tau \approx 100$ MPa), for grainsize $D \leq 100$ nm (Fig. 9b). Under
437 these conditions, the shear stress values measured during our laboratory experiments are
438 between the calculated flow stress values for grainsize 10 < D < 100 nm (Fig. 9b).
439 Our microstructural observations suggest that brittle fracturing and cataclasis are the
440 mechanisms that control shear localisation and grain size reduction in the slip zone at
441 relatively low temperatures (≤ 100 °C). Stress levels predicted by Byerlee's sliding friction
442 values (Byerlee, 1978) match those measured during Stage I (Fig. 10). Very little is known
443 about how grain size reduction to submicron levels actually occurs under the conditions
444 attained during our experiments ($T \geq 500$ °C), where samples have been deformed up to Stage
445 II (Green et al., 2015; Verberne et al., 2013, 2014). Here, we propose that, as temperatures
446 rise during Stage II, due to frictional heating (≥ 500 °C), dislocation creep mechanisms start
447 to accommodate intragranular strain and play a key role in producing nanoscale subgrains
448 ($D \leq 100$ nm) in the slip zone (Fig. 4). Note that during Stage II, nanoparticles are present in
449 the slip zone and seismic slip rates have been attained. However, the measured frictional

strength of the experimental faults still lies within Byerlee's range of values μ = 0.68 -0.80 (Fig. 1, Supplementary Information Table I). In the absence of microstructural evidence for the operation of pressure solution or diffusion creep (e.g., Verberne et al., 2014), it is suggested that the slip zone bulk strength at this stage is still controlled by cataclastic frictional sliding rather than by dislocation creep or nanopowder lubrication mechanisms. This is in accord with our flow stress calculations, which predict flow stresses for dislocation creep that are up to about 3 orders of magnitude higher than the measured ones at T = 600 °C and $\dot{\gamma} \geq 1*10^2$ s^{-1} (Figs. 9a, 10). When $T \approx$ 1000 °C and $\dot{\gamma} \approx 3*10^3$ s^{-1} are attained during Stage III, micro-textures diagnostic of both dislocation creep and grainsize-sensitive GBS are observed, the latter becoming widespread within the slip zone (Fig. 5). Under these temperature and strain rate conditions, the flow stresses predicted for grainsize-sensitive GBS-accommodated flow, for grain size D < 100 nm observed in the slip zone at the onset of weakening, are lower than those predicted by Byerlee's friction and, within the same order of magnitude as the values measured during the experiments (Fig. 10).

Our microstructural observations are similar to those of previous studies showing that, under certain conditions, fine-grained geological materials deform by diffusion-accommodated GBS and dislocation-accommodated GBS (Schmid et al., 1977; Walker et al., 1990). This combination of mechanisms appears to be capable of explaining not only the observed relation between strain rate and stress (Schmid et al., 1977; Walker et al., 1990; Hirth and Kohlstedt, 2003; Mecklenburgh et al., 2010; Goldsby and Kohlstedt, 2001), but also most of the microstructural and topological features of materials displaying superplastic behaviour (Ashby and Verrall, 1973; Schmid et al., 1977; Walker et al., 1990; Hirth and Kohlstedt, 2003; Mecklenburgh et al., 2010; Goldsby and Kohlstedt, 2001; Verberne et al., 2015; Green et al., 2015).

474 We propose therefore that the activation of grainsize-sensitive GBS deformation
475 mechanisms in the nanograin aggregates (D < 100 nm) of the localised slip zone, at high
476 temperatures ($T \approx 1000$ °C) and strain rates $\dot{\gamma} \geq 1000\ s^{-1}$, controls the onset of dynamic
477 weakening of carbonate faults at seismic slip rates (Fig. 10). Note, however, that the cataclasis
478 and intragranular dislocation creep operating during the earlier stages of slip are critical,
479 precursory processes needed to produce the nanoscale grain sizes required to activate
480 grainsize-sensitive creep mechanisms. Finally, the re-strengthening observed during the
481 decelerating phase of deformation can be explained by the falling temperature "switching off"
482 slip zone-localised GBS flow, leading to a return to frictional sliding.

483 **6.2.3 Limitations and approximation of flow stress calculations and interpretations**

484 The calculated flow stress values have been obtained by extrapolating published
485 constitutive flow laws for grainsize-sensitive GBS in carbonates to the conditions attained
486 during our experiments (Fig. 9, Tables I). The flow stress values obtained for the
487 temperatures, strain rates and grain sizes attained during our experiments, at the onset of
488 weakening, are within about one order of magnitude of those measured during our
489 experiments (Figs. 9-10). The remaining discrepancies are likely due to the approximation of
490 the estimated slip zone parameters (e.g., grain size and SZ thickness), the experimental
491 conditions (γ), and the simplistic extrapolation of existing flow laws to smaller, sub-micron
492 grain sizes and to strain rates which are a few orders of magnitude higher than those at which
493 they were obtained.

494 In our study we provide evidence that the onset of weakening during shearing at high
495 velocity coincides with the activation of thermally-induced deformation mechanisms (e.g.,
496 grainsize-sensitive GBS) within thin layers of nanograins sandwiched by slip surfaces. To a
497 first approximation, the measured drop in strength is in agreement with our flow stress
498 calculations, suggesting that strain could be accommodated more efficiently by these

mechanisms within the weaker thin layers than by frictional sliding along the SS (Fig. 5b-c). A quantitative estimation of the strain partitioning between sliding along the SS and deformation within the thin layers will allow the conceptual model described above to be proven, and provide more constrained strain rate values to be applied in the flow stress calculations. At the present stage, these tasks still present some significant practical challenges in rotary shear apparatus experiments and advanced microstructural studies on the deformed materials.

7. Conclusions

Our observations of experimentally and naturally produced carbonate faults suggest that grainsize-sensitive GBS deformation mechanisms can operate in geological materials deformed at high strain rates along frictionally heated seismogenic slip surfaces at the onset of dynamic weakening after a few centimetres of slip (d > 10 cm), before the occurrence of bulk phase transformations. The observed microstructures are similar to those seen at low and high strain rates in carbonates (Verberne et al., 2014; Green et al., 2015), and at high strain rates for a range of nano-phase alloys and ceramics in association with superplastic behaviour, where grainsize-sensitive creep regimes develop due to the combined operation of dislocation/diffusion creep. Our findings provide a plausible explanation for both the low flow stresses measured at seismic slip rates in carbonate rocks, and most of the microstructural and topological features of the deformed materials. A regime of frictionally-induced grainsize-sensitive GBS can thus account for the self-lubrication and dynamic weakening of carbonate faults during earthquake propagation in nature.

Acknowledgements

This study was supported by the Natural Environment Research Council (NERC Standard Grant NE/H021744/1 awarded to NDP and REH), and the ERC Starting Grant GLASS no. (259256). L. Bowen (G.J. Russell Microscopy Facility, Durham University, UK) provided

524 invaluable assistance during SEM and TEM analyses. J. Mecklenburgh, L. Hansen and C.
525 Spiers are thanked for providing helpful comments improving the quality of the text and of
526 our interpretations.

527 **References**

528 Ashby, M.F., Verrall, R.A., 1973. Diffusion-Accommodated Flow and Superplasticity. Acta
529 Metallurgica 21, 149-163.
530 Ashby, M.F.a.V., R.A., 1977. Micromechanics of flow and fracture, and their relevance to the
531 rheology of the upper mantle. Philosophical Transactions of the Royal Society of London
532 288, 59-95.
533 Bullock, R.J., De Paola, N., Holdsworth, R.E., Trabucho-Alexandre, J., 2014. Lithological
534 controls on the deformation mechanisms operating within carbonate-hosted faults during the
535 seismic cycle. J. Struct. Geol. 58, 22-42.
536 Bullock, R.J., De Paola, N. & Holdsworth, R.E., 2015. An experimental investigation into the
537 role of phyllosilicate content on earthquake propagation during seismic slip in carbonate
538 faults. Journal of Geophysical Research: Solid Earth 120(5), 3187-3207.
539 Boullier, A.M., Gueguen, Y., 1975. Sp-Mylonites - Origin of Some Mylonites by Superplastic
540 Flow. Contrib Mineral Petr 50, 93-104.
541 Byerlee, J., 1978. Friction of Rocks. Pure Appl Geophys 116, 615-626.
542 Chandra, N., 2002. Constitutive behavior of superplastic materials. International Journal of
543 Non-Linear Mechanics 37, 461-484.
544 Collettini, C., Viti, C., Tesei, T., Mollo, S., 2013. Thermal decomposition along natural faults
545 during earthquakes. Geology 41, 927e930. http://dx.doi.org/10.1130/G34421.1.
546 Collettini, C., Carpenter, B.M., Viti, C., Cruciani, F., Mollto, S., Tesei, T., Trippetta, F.,
547 Valoroso, L., Chiaraluce, L., 2014. Fault structure and slip localization in carbonate bearing

548 normal faults: an example from the Northern Apennines of Italy. J. Struct. Geol. 67, 154–166.
549 http://dx.doi.org/10.1016/j.jsg.2014.07.017.
550 Covey-Crump, S.J., 1997. The normal grain growth behaviour of nominally pure calcitic
551 aggregates. Contribution to Mineralogy and Petrology 129, 239-254.
552 De Paola, N., Collettini, C., Faulkner, D.R., Trippetta, F., 2008. Fault zone architecture and
553 deformation processes within evaporitic rocks in the upper crust. Tectonics 27.
554 http://dx.doi.org/10.1029/2007TC002230.
555 De Paola, N., Chiodini, G., Hirose, T., Cardellini, C., Caliro, S. & Shimamoto, T., 2011a. The
556 geochemical signature caused by earthquake propagation in carbonate-hosted faults. Earth
557 and Planetary Science Letters 310(3-4), 225-232.
558 De Paola, N., Hirose, T., Mitchell, T., Di Toro, G., Viti, C., Shimamoto, T., 2011b. Fault
559 lubrication and earthquake propagation in thermally unstable rocks. Geology 39, 35-38.
560 De Paola, N., 2013. Nano-powder coating can make fault surfaces smooth and shiny:
561 implications for fault mechanics? Geology 41, 719-720.
562 Di Toro, G., Han, R., Hirose, T., De Paola, N., Nielsen, S., Mizoguchi, K., Ferri, F., Cocco,
563 M., Shimamoto, T., 2011. Fault lubrication during earthquakes. Nature 471, 494-+.
564 Fondriest, M., Smith, S.A.F., Candela, T., Nielsen, S.B., Mair, K., Di Toro, G., 2013. Mirror-
565 like faults and power dissipation during earthquakes. Geology 41, 1175-1178.
566 Goldsby, D. L., Kohlstedt, D. L., 2001. Superplastic deformation of ice: Experimental
567 observations.J Geophys Res-Sol Ea 106, 11017-11030.
568 Goldsby, D.L., Tullis, T.E., 2011. Flash Heating Leads to Low Frictional Strength of Crustal
569 Rocks at Earthquake Slip Rates. Science 334, 216-218.
570 Green, H.W., Shi, F., Bozhilov, K., Xia, G., Reches, Z., 2015. Phase Transformation and
571 Nanometric Flow Cause Extreme Weakening During Faulting. Nature Geoscience DOI:
572 10.1038/NGEO2436.

573 Han, R., Hirose, T., Shimamoto, T., 2010. Strong velocity weakening and powder lubrication
574 of simulated carbonate faults at seismic slip rates. J Geophys Res-Sol Ea 115, -.
575 Hiraga, T., Miyazaki, T., Tasaka, M., Yoshida, H., 2010. Mantle superplasticity and its self-
576 made demise. Nature 468, 1091-U1490.
577 Hirose, T., Shimamoto, T., 2005. Growth of molten zone as a mechanism of slip weakening
578 of simulated faults in gabbro during frictional melting. J Geophys Res-Sol Ea 110, -.
579 Hirth, G., and D. L. Kohlstedt, 2003. Inside the subduction factory edited by J. Eiler, pp. 83-
580 105, American Geophysical Union, Washington D. C.
581 Kohlstedt, D.L., Evans, B., Mackwell, S.J., 1995. Strength of the Lithosphere - Constraints
582 Imposed by Laboratory Experiments. J Geophys Res-Sol Ea 100, 17587-17602.
583 Lankford, J., 1996. High strain rate compression and plastic flow of ceramics. Journal of
584 Materials Science Letters 15, 745-750.
585 Mecklenburgh, J., Heidelbach, F., Mariani, E., Mackwell, S. and Seifert, F., 2010. Rheology
586 and microstructure of (Ca0.9,Sr0.1)TiO3 perovskite deformed in compression and torsion. J
587 Geophys Res-Sol Ea 115.
588 Olgaard, D. L., Evans, B., 1986. Effect of second-phase particles on grain growth in calcite.
589 Contribution to Mineralogy and Petrology, 69, C272-C277.
590 Passchier, C.W.a.T., R.A.J., 2005. Micro-tectonics. Springer, 1-365.
591 Poirier, J.P., 1985. Creep of Crystals. Cambridge Earth Sciences Series, 1-258.
592 Reches, Z., Lockner, D.A., 2010. Fault weakening and earthquake instability by powder
593 lubrication. Nature 467, 452-U102.
594 Ree, J.H., Ando, J.I., Han, R., Shimamoto, T., 2014. Coseismic microstructures of
595 experimental fault zones in Carrara marble. J Struct Geol 66, 75-83.
596 Rice, J.R., 2006. Heating and weakening of faults during earthquake slip. J Geophys Res-Sol
597 Ea 111, -.

598 Rowe, C.D., Fagereng, A., Miller, J.A., and Mapani, B., 2012. Signature of coseismic
599 decarbonation in dolomitic fault rocks of the Naukluft Thrust, Namibia. Earth and Planetary
600 Science Letters 333, 200–210. doi:10.1016/j.epsl .2012.04.030.
601 Rutter, E.H., 1995. Experimental study of the influence of stress, temperature, and strain on
602 the dynamic recrystallization of Carrara marble. J Geophys Res-Sol Ea 100, 24651-24663.
603 Rutter, E.H., 1999. On the relationship between the formation of shear zones and the form of
604 the flow law for rocks undergoing dynamic recrystallization. Tectonophysics 303, 147-158.
605 Rutter, E.H., Brodie, K.H., 1988. The Role of Tectonic Grain-Size Reduction in the
606 Rheological Stratification of the Lithosphere. Geol Rundsch 77, 295-307.
607 Rutter, E.H., Casey, M., Burlini, L., 1994. Preferred Crystallographic Orientation
608 Development during the Plastic and Superplastic Flow of Calcite Rocks. J Struct Geol 16,
609 1431-1446.
610 Schmid, S.M., Boland, J.N., Paterson, M.S., 1977. Superplastic Flow in Finegrained
611 Limestone. Tectonophysics 43, 257-291.
612 Scholz, C.H., 1998. Earthquakes and friction laws. Nature 391, 37-42.
613 Schubnel, A., Brunet, F., Hilairet, N., Gasc, J., Wang, Y.B., Green, H.W., 2013. Deep-Focus
614 Earthquake Analogs Recorded at High Pressure and Temperature in the Laboratory. Science
615 341, 1377-1380.
616 Sibson, R.H., 1977. Fault rocks and fault mechanisms. J Geol Soc London 133, 191-213.
617 Siman-Tov, S., Aharonov, E., Sagy, A., Emmanuel, S., 2013. Nanograins form carbonate
618 fault mirrors. Geology 41, 703-706.
619 Smith, S.A.F., Billi, A., Di Toro, G., Spiess, R., 2011. Principal slip zones in limestone:
620 microstructural characterization and implications for the seismic cycle (Tre Monti Fault,
621 Central Apennines, Italy). Pure Appl. Geophys. 168, 2365e2393.
622 http://dx.doi.org/10.1007/s00024-011-0267-5.

623 Smith, S.A.F., Di Toro, G., Kim, S., Ree, J.H., Nielsen, S., Billi, A., Spiess, R., 2013.
624 Coseismic recrystallization during shallow earthquake slip. Geology 41, 63-66.
625 Smith, S.A.F., Nielsen, S., Di Toro, G., 2015. Strain localization and the onset of dynamic
626 weakening in calcite fault gouge. Earth Planet. Sc. Lett. 413, 25-36.
627 Tisato, N., Di Toro, G., De Rossi, N., Quaresimin, M., Candela, T., 2012. Experimental
628 investigation of flash weakening in limestone. J Struct Geol 38, 183-199.
629 Valoroso, L., Chiaraluce, L., Collettini, C., 2014. Earthquakes and fault zone structure.
630 Geology 42, 343-346.
631 Verberne, B.A., Plümper, O., Matthijs de Winter, D.A. and Spiers, C.J., 2014. Superplastic
632 nanofibrous slip zones control seismogenic fault friction. Science 346, ISSUE 6215.
633 Verberne, B. A., De Bresser, J. H. P., Niemeijer, A. R., Spiers, C. J., De Winter, D. A. M.,
634 and Plumper, O., 2013. Nanocrystalline slip zones in calcite fault gouge show
635 intense crystallographic preferred orientation: Crystal plasticity at sub-seismic slip rates at 18
636 – 150 C. Geology 41, 863–866.
637 Walker, A.N., Rutter, E.H., Brodie, K.H., 1990. Experimental-Study of Grain-Size Sensitive
638 Flow of Synthetic, Hot-Pressed Calcite Rocks. Deformation Mechanisms, Rheology and
639 Tectonics 54, 259-284.

640 **Figure Captions:**

641 **Figure 1 – Experimental data.** a-b) Slip rate vs. displacement data for a set of displacement-
642 controlled experiments performed at σ_n = 12, 18 MPa, and arrested before, during and after
643 the attainment of target speed, v = 1 ms^{-1}. c-d) Friction coefficient vs. displacement data
644 showing the evolution of friction during acceleration (Stages I-II), steady-state sliding (Stage
645 III) and instantaneous deceleration to arrest (Stage IV) of the sample. The inset shows a blow-
646 up of the data in the main graph.

Figure 2 – Temperature vs. friction coefficient data. Temperatures calculated for localised, thin (< 150 μm) slip zones plotted vs. the friction coefficient measured during laboratory experiments performed at seismic, target slip rates (1 ms^{-1}) on carbonate gouges (Table I).

Figure 3: **Microstructural observations of experimental slip zones (Stage I).** a) Scanning electron microscope (SEM) image showing in plan view the development of a rough SS, due to the presence of grooves (g) and ridges (r), oriented parallel to the slip direction. b) Optical microscope image showing in cross-section the formation of a continuous, immature slip zone (SZ) with variable thickness (20-200 μm), bounded on the upper part by a rough SS. c) SEM image in plan view showing a magnified, smooth portion of the SS made of fine-grained clasts ($1 < D < 5$ μm), which are sharply truncated against the SS.

Figure 4 – Microstructural observations of experimental slip zones (Stage II). a-c) Optical microscope (a, cross section view) and SEM (b-c, plan view) images show the development a cohesive slip zone (SZ), and striated slip surface (SS) sandwiching thin layers made of nanograin aggregates (D ≤ 100 nm) with sub-rounded shape. d) TEM image showing calcite nanograins (≤ 100 nm) in contact with a calcite clast (CC) hosting dislocations and dislocation walls (DW) separating subgrains (SG) ($D \leq 100$ nm). e) Calcite clasts (CC) exhibit "damaged" rims, hosting rounded bubbles and lobate, low-contrast features (arrows) (Bright-field TEM images). d) Measured d-spacings from ring-shaped SAED pattern confirm that ultrafine grains are formed by calcite.

Figure 5 – Microstructural observations of experimental slip zones (Stage III). a-c) Optical microscope (a, cross section and inset oblique plan views) and SEM (b-c, plan view) images show the development of a cohesive slip zone (SZ) composed of stacked striated slip surfaces (SS), sandwiching thin layers (tl) of nanoscale grains. d) TEM images show that tl are associated with compact polygonal nanostructures of calcite grains, displaying low free dislocation densities. e) TEM image of relatively large cavities (C) formed along grain

672 boundaries or at triple junctions, whereas smaller rounded bubbles are trapped within calcite
673 grains (B). f) Calcite clast relic from the thin porous layers in the slip zone (see main text),
674 exhibiting irregular, lobate crystal boundaries, surrounded by a 10 nm thick amorphous rim
675 (am). g) Measured d-spacings from single-crystal SAED pattern of polygonal grains from the
676 thin layers confirm that polygonal grains are formed by calcite (arrows show the
677 corresponding reciprocal axes).
678 **Figure 6 – Modelled grainsize vs. time during static crystallization.** The graph shows the
679 maximum, theoretical increase in grain size, obtained by solving Eq. 2 in the main text for
680 range of temperatures, initial grain sizes and timescales representative of those attained during
681 sample deformation up to Stage II (T = 500 °C) and Stage III (T = 800 - 1000 °C). The blue
682 (Stage II) and black (Stage III) rectangles show the range of grainsizes observed in the
683 experimental slip zones.
684 **Figure 7 – Mesoscale and microstructural observations from natural slip zones.** a)
685 Outcrop photograph of the M. Maggio fault plane, located in the Apennines of Italy (details in
686 Collettini et al., 2014), showing its naturally polished, reflective glossy surface. b) Rock
687 sample cross section including hanging-wall, HW, and footwall, FW, blocks together with the
688 principal slipping zone (indicated by the arrow) where we performed the microstructural
689 studies. c) BSE-SEM image in cross section showing that the principal slipping zone is about
690 100 mm thick (dashed yellow line) and, here, the slip is accommodated along sub-parallel SSs
691 indicated by yellow arrows. d) Nanostructure composed of polygonal calcite grains in close
692 association with strain-free calcite crystals.
693 **Figure 8 – Microstructures diagnostic of superplastic behavior: theory vs.**
694 **experimental/natural slip zone samples.** a-b) SEM images of experimental (a) and natural
695 (b) slip zones made of compact calcite nanograin aggregates with a polygonal texture,
696 diagnostic of grainsize sensitive grain boundary sliding (GBS) mechanisms. c) Diagnostic

697 microstructures predicted by superplastic flow accommodated by grainsize sensitive GBS,
698 showing different stages (I-III) of the neighbour switching process (after Ashby and Verrall,
699 1973).
700 **Figure 9 – Measured and predicted flow stresses.** a-b) Calculated flow stresses for
701 dislocation creep and grainsize sensitive GBS creep (Eq. 2 in the main text) are plotted vs.
702 strain rates for a range of grain sizes (GBS only) and temperatures, representative of the
703 conditions attained during sample deformation up to Stage II (a) and Stage III (b). The green
704 dots represent the measured shear stress attained in our experiments at steady state during
705 deformation up to Stage III.
706 **Figure 10 – Fault strength evolution with increasing temperatures at high strain rates.**
707 Shear stresses predicted by frictional sliding (Byerlee, 1978) match those measured during
708 laboratory experiments at seismic slip rates during Stages I-II (temperature ≤ 600 °C). Flow
709 stress values predicted by a regime of grainsize-sensitive GBS creep (Eq. 2 constitutive law in
710 the main text) at temperatures ≥ 600 °C, strain rates = $3*10^3$ s^{-1} and grainsize D < 100 nm,
711 observed in the slip zone at the onset of weakening, are lower than those predicted by
712 Byerlee's friction, and within the same order of magnitude as the values measured during the
713 experiments during Stage III.
714
715
716
717
718
719
720
721

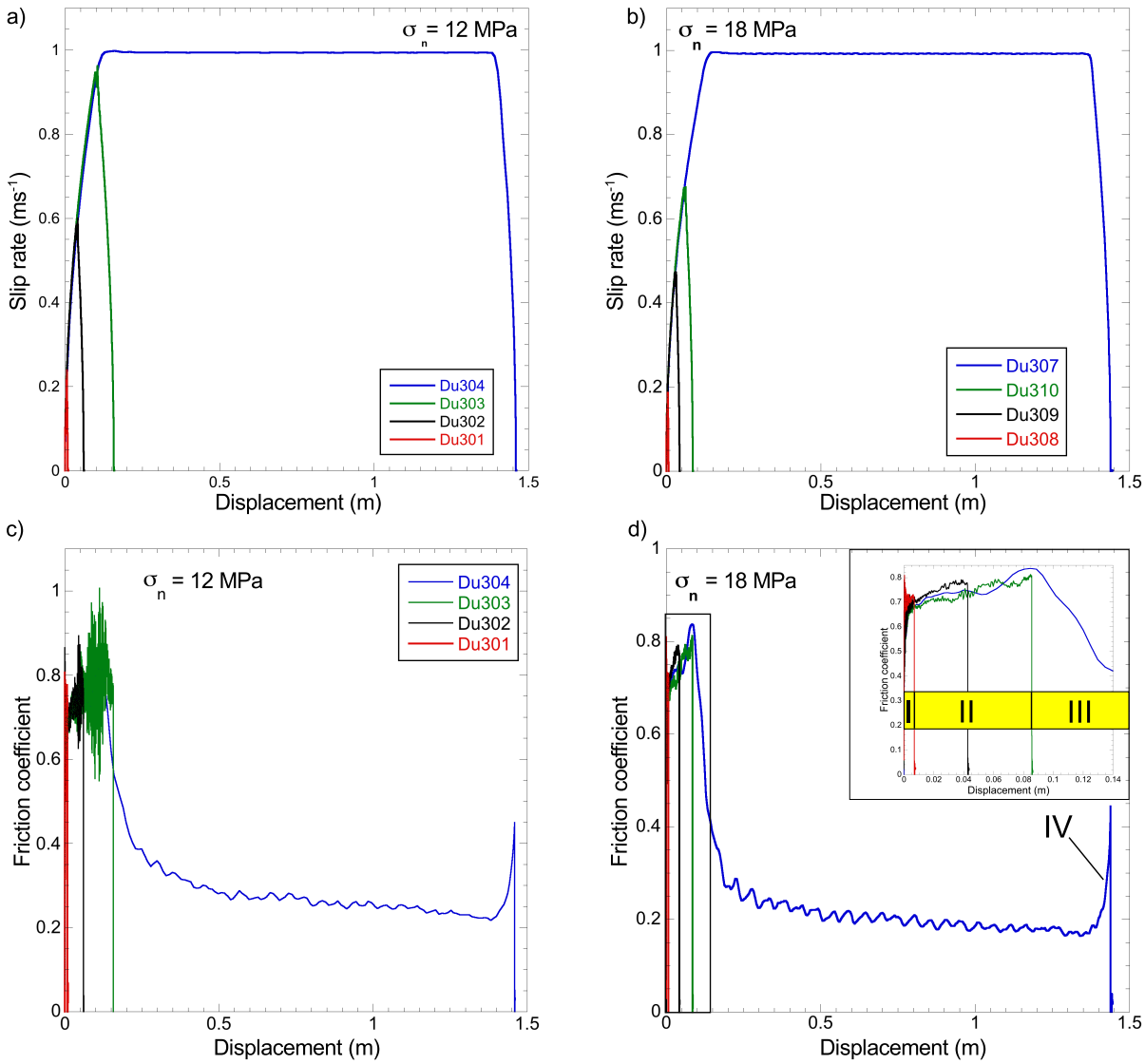

722

723 Figure 1

724

725

726

727

728

729

730

731

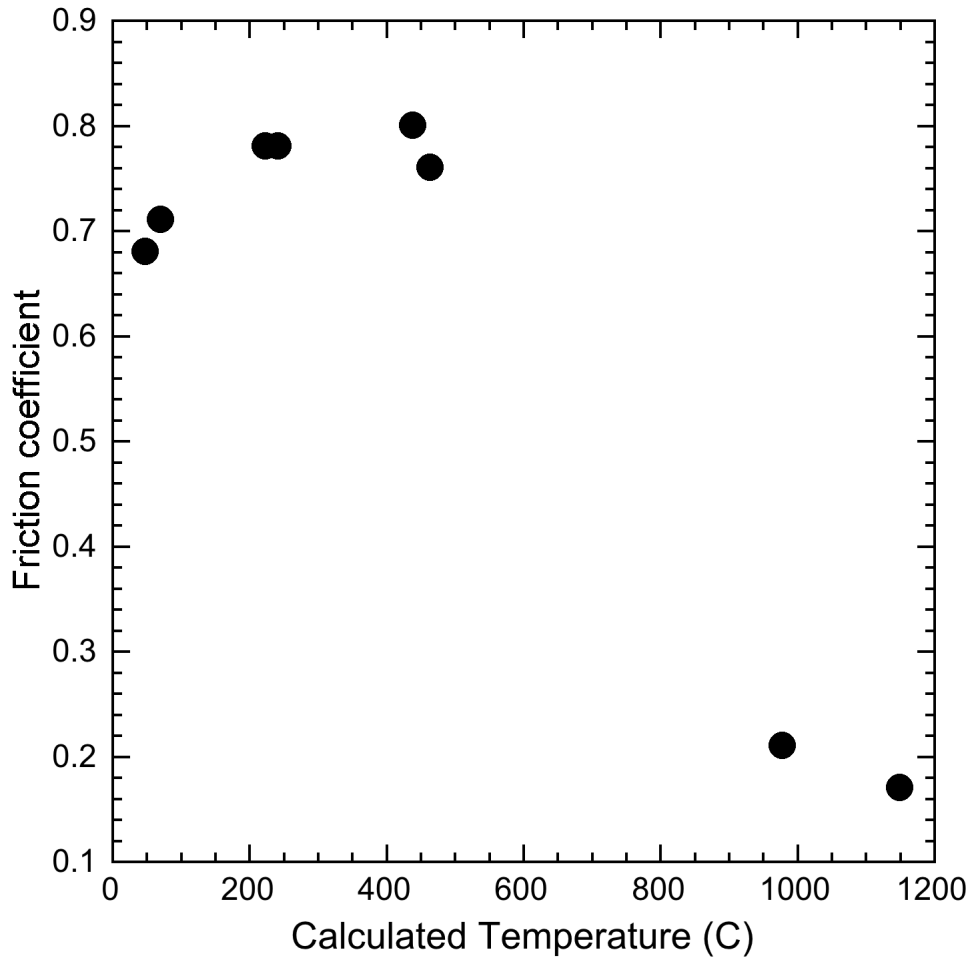
Friction coefficient
Calculated Temperature (C)
0.9
0.8
0.7
0.6
0.5
0.4
0.3
0.2
0.1
0
200
400
600
800
1000
1200

Figure 2

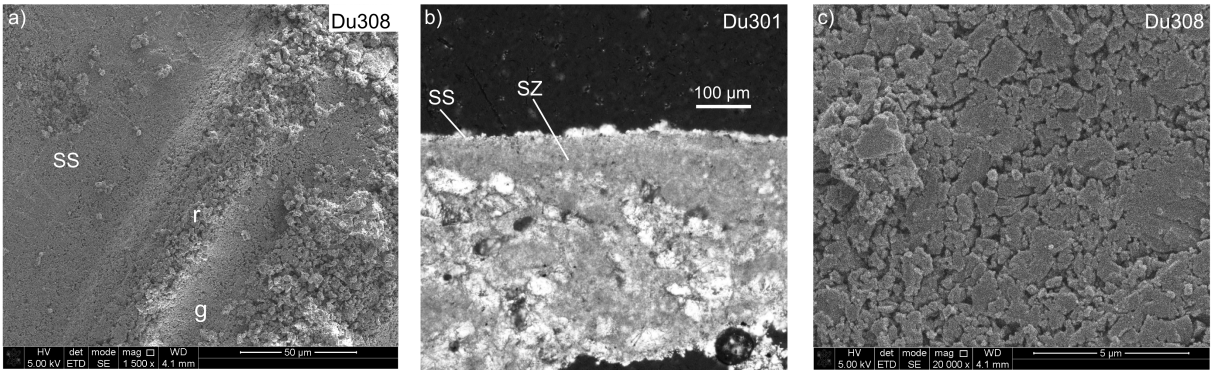
a)
Du308
SS
r
g
HV 5.00 kV
det ETD
mode SE
mag 1 500 x
WD 4.1 mm
50 µm
b)
Du301
SS
SZ
100 µm
c)
Du308
HV 5.00 kV
det ETD
mode SE
mag 20 000 x
WD 4.1 mm
5 µm

Figure 3

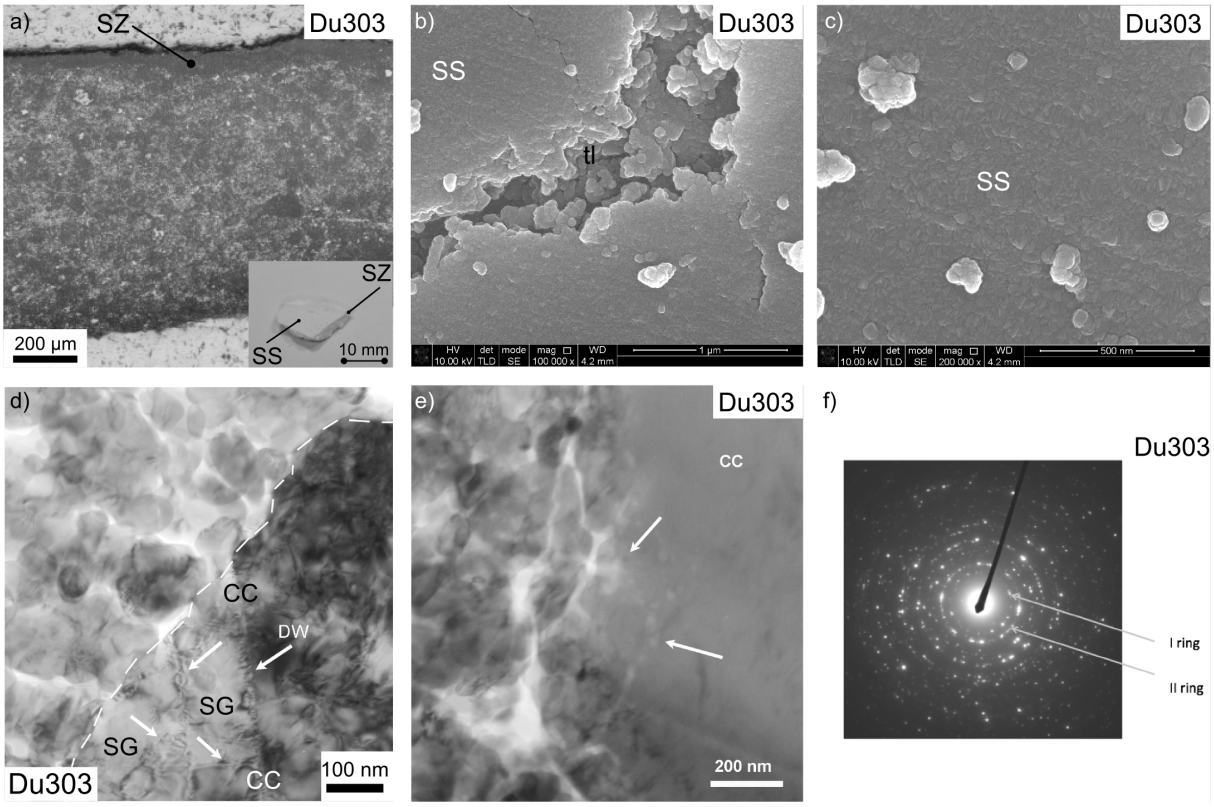
a)
SZ
Du303
200 μm
SZ
SS
10 mm
b)
Du303
SS
tl
c)
Du303
SS
d)
CC
DW
SG
SG
Du303
CC
100 nm
e)
Du303
cc
200 nm
f)
Du303
I ring
II ring

Figure 4

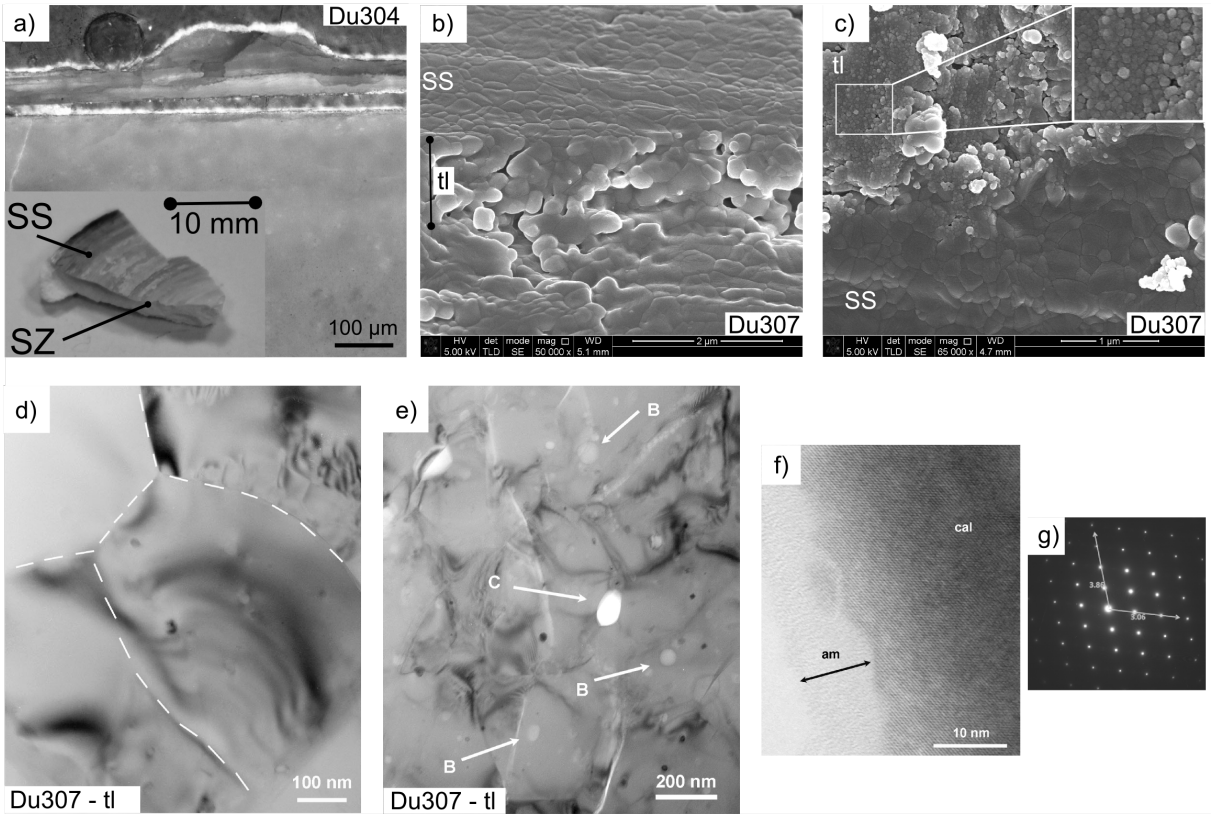
a)
Du304
SS
10 mm
SZ
100 µm
b)
SS
tl
Du307
c)
tl
SS
Du307
d)
100 nm
Du307 - tl
e)
B
C
B
B
200 nm
Du307 - tl
f)
cal
am
10 nm
g)

Figure 5

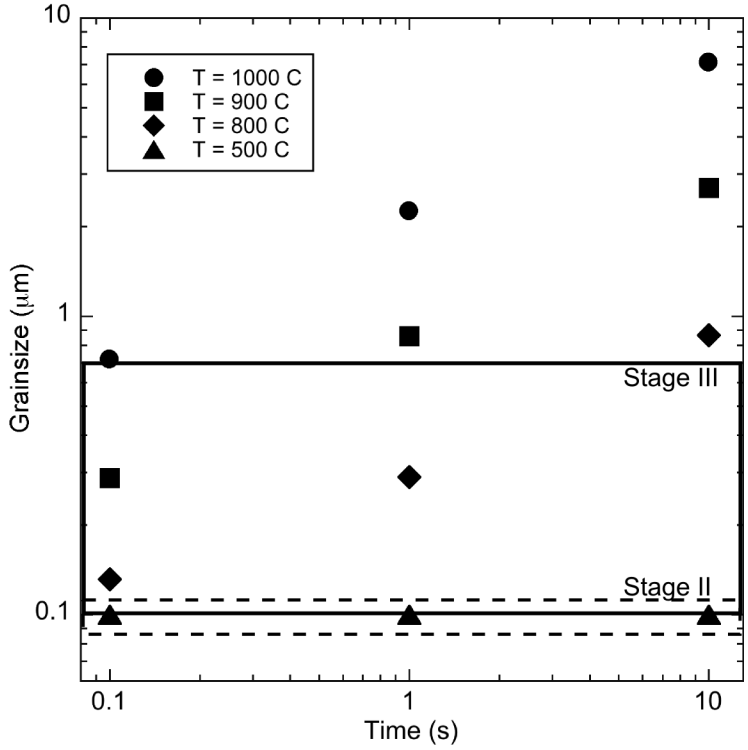
T = 1000 C
T = 900 C
T = 800 C
T = 500 C
Grainsize (μm)
10
1
0.1
Stage III
Stage II
0.1
1
10
Time (s)

Figure 6

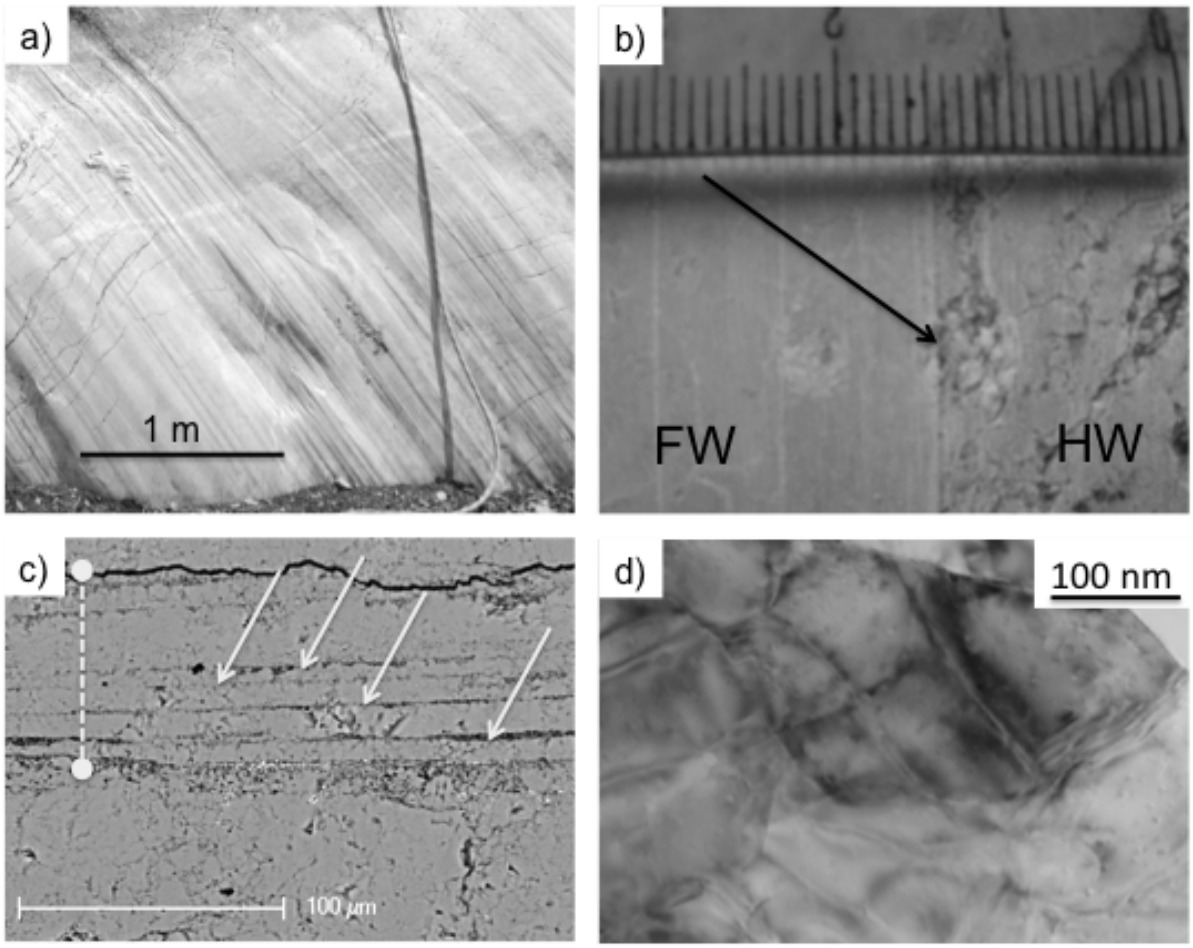

Figure 7

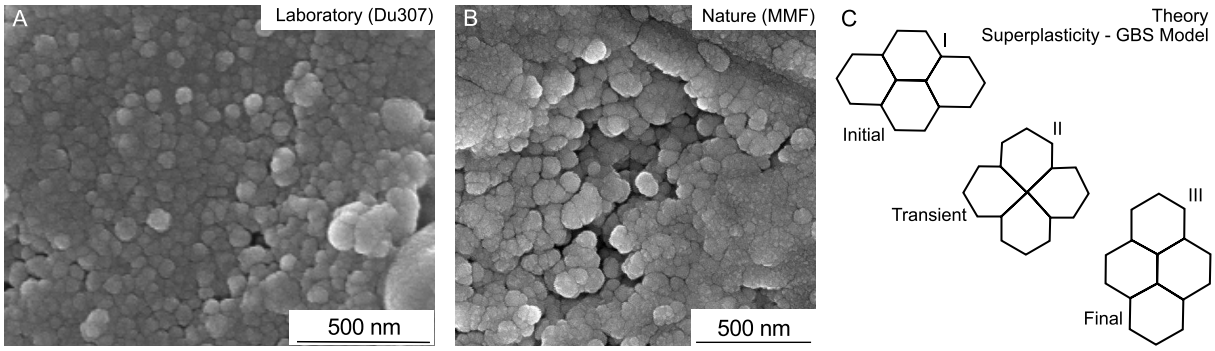
A
Laboratory (Du307)
500 nm
B
Nature (MMF)
500 nm
C
Theory
Superplasticity - GBS Model
I
Initial
II
Transient
III
Final

Figure 8

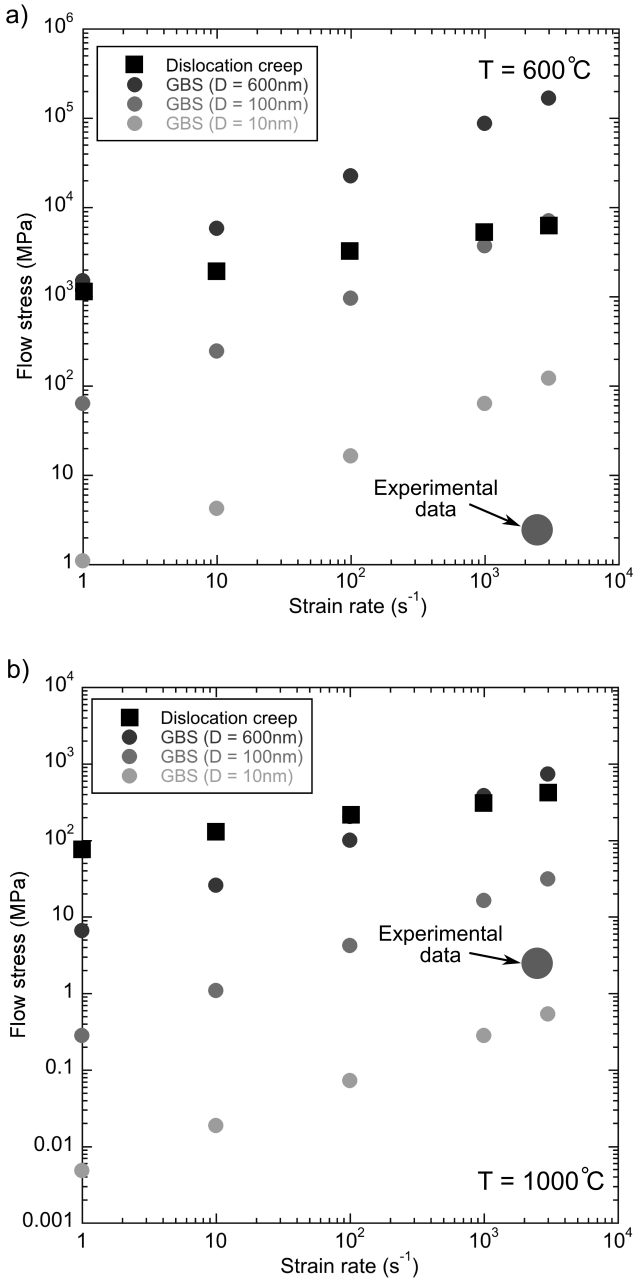
a)
Dislocation creep
GBS (D = 600nm)
GBS (D = 100nm)
GBS (D = 10nm)
T = 600℃
Experimental data
Flow stress (MPa)
Strain rate (s-1)
b)
Dislocation creep
GBS (D = 600nm)
GBS (D = 100nm)
GBS (D = 10nm)
Experimental data
T = 1000℃
Flow stress (MPa)
Strain rate (s-1)

Figure 9

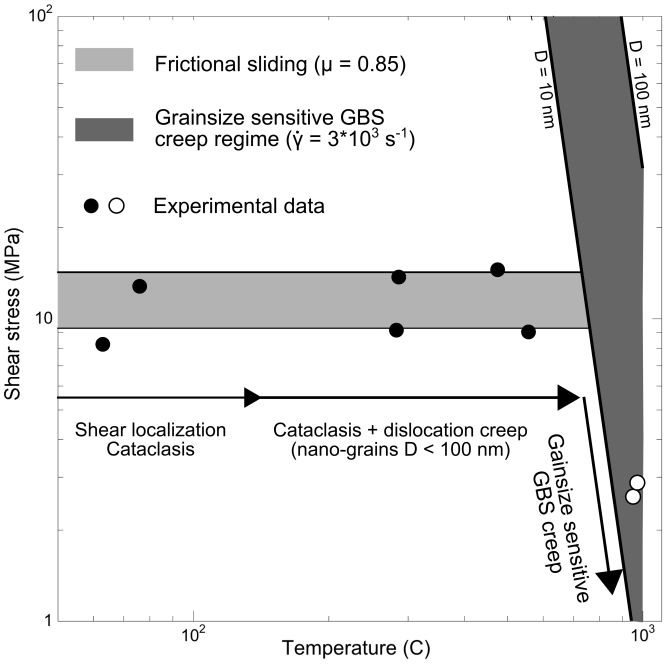

938
939
940 Figure 10